Idealized large-eddy simulations of stratocumulus advecting over cold water. Part 1: Boundary layer decoupling

Youtong Zheng[1], Haipeng Zhang[1], Daniel Rosenfeld[2], Seoung-Soo Lee[1], Tianning Su[1], and Zhanqing Li[1]

Affiliations:

[1]Earth System Science Interdisciplinary Center, University of Maryland, College Park, Maryland, 20742, USA.

[2]Herew University of Jerusalem, Jerusalem, Isreal

Corresponding author: Youtong Zheng, Earth System Science Interdisciplinary Center, University of Maryland, College Park, Maryland, 20742, USA, zhengyoutong@gmail.com

Abstract

We explore the decoupling physics of a stratocumulus-topped boundary layer (STBL) moving over cooler water, a situation mimicking the warm air advection (WADV). We simulate an initially well-mixed STBL over a doubly periodic domain with the sea surface temperature decreasing linearly over time using the System for Atmospheric Modeling large-eddy model. Due to the surface cooling, the STBL becomes increasingly stably stratified, manifested as a near-surface temperature inversion topped by a well-mixed cloud-containing layer. Unlike the stably stratified STBL in cold air advection (CADV) that is characterized by cumulus coupling, the stratocumulus deck in the WADV is unambiguously decoupled from the sea surface, manifested as weakly negative buoyancy flux throughout the sub-cloud layer. Without the influxes of buoyancy from the surface, the convective circulation in the well-mixed cloud-containing layer is driven by cloud-top radiative cooling. In such a regime, the downdrafts propel the circulation, in contrast to that in CADV regime for which the cumulus updrafts play a more determinant role. Such a contrast in convection regime explains the difference in many aspects of the STBLs including the entrainment rate, cloud homogeneity, vertical exchanges of heat and moisture, and lifetime of the stratocumulus deck, with the last being subject to a more thorough investigation in part 2 of this study. Finally, we investigate under what conditions a secondary stratus near the surface (or fog) can form in the WADV. We found that weaker subsidence favors the formation of fog whereas a more rapid surface cooling rate doesn't.

Significant statement

The low-lying blanket-like clouds, called stratocumulus (Sc), reflect much incoming sunlight, substantially modulating the Earth's temperature. While much is known about how the Sc evolves when it moves over warmer water, few studies examine the opposite situation of Sc moving over colder water. We used a high-resolution numerical model to simulate such a case. When moving over cold water, the Sc becomes unambiguously decoupled from the water surface, distinctive from its warm counterpart in which the Sc interacts with the water surface via intermittent cauliflower-like clouds called cumulus clouds. Such decoupling influences many aspects of the Sc-sea-surface system, which combine to alter the ability of the Sc to reflect sunlight, thereby influencing the climate. This work laid the foundation for future work that quantifies the contribution of such a decoupled Sc regime to the Earth's radiative budget and climate change.

1. Introduction

Marine stratocumulus (Sc) significantly alters the Earth's radiative budgets at both the surface and the top of the atmosphere (Hartmann et al., 1992; Hahn and Warren, 2007; Wood, 2012). The Sc strongly interacts with the marine boundary layer. The interactions manifest as exchanges of heat, moisture, and mass between the stratocumulus and the sea surface, forming a coupled Sc-surface system commonly known as the stratocumulus-topped planetary boundary layer (STBL). The earliest credible description of the STBL physics is Lilly (1968)'s mixed-layer model. The model treats the column of air from the surface to the top of Sc as a well-mixed bulk layer and parameterizes basic cloud physics and fluxes (i.e. energy, moisture, and mass). The model succeeds in explaining a series of important behaviors of STBL over the subtropical oceans such as the STBL response to large-scale environment (Schubert et al., 1979a, b; Wakefield and Schubert, 1981; Stevens, 2006), the STBL decoupling during the cloud regime transition (Bretherton and Wyant, 1997; Zheng et al., 2020), diurnal cycle (Caldwell et al., 2005; Zhang et al., 2005), dominant time scales (Jones et al., 2014), slow manifold behavior (Bretherton et al., 2010), and aerosol influences on Sc (Wood, 2007; Caldwell and Bretherton, 2009; Uchida et al., 2010).

The Lily's mixed-layer model becomes invalid if the STBL stably stratifies, a phenomenon widely known as STBL decoupling (Nicholl, 1984). The decoupling physics can be understood from the perspective of boundary layer energetics. In a well-mixed STBL over cold water, air parcels entrained from the overlying inversion are cooled by thermal radiation at the cloud top, sinking through the boundary layer. This well-mixed state is sustained by a rough balance between entrainment warming and radiative cooling in the upper part of the STBL. When the warming outweighs the cooling, the entrained warm airs are too light to sink, leading to the

85 stable stratification of the boundary layer. Examples include the decoupling during the
86 subtropical stratocumulus-to-cumulus transition due to enhanced entrainment warming
87 (Bretherton and Wyant, 1997), decoupling by precipitation that warms the cloud layer (Nicholls,
88 1984; Stevens et al., 1998), and daytime decoupling by solar insolation that weakens cloud-top
89 radiative cooling (Nicholls and Leighton, 1986; Zheng et al., 2018).

90 The above decoupling mechanisms have been studied in subtropical conditions where the
91 trade winds advect the STBL toward the equator with warmer surfaces. The cold air advection
92 builds up the potential energy of the environment so that the decoupled STBLs are typically
93 conditionally unstable. This allows for the development of cumulus (Cu) that often penetrates the
94 Sc decks, forming Cu-coupled STBLs. In such a cloud regime, the Sc can interact with the
95 surface through the conduits of the Cu convection so that whether or not to call the boundary
96 layer "decoupled" has been controversial (Miller and Albrecht, 1995; Stevens et al., 1998; Goren
97 et al., 2018a; Zheng et al., 2018; Zheng and Li, 2019).

98 To reconcile the controversy, Zheng et al. (2020) added a new dimension, namely low-
99 level temperature advection, to the problem. Zheng et al. (2020) considered the coupling state of
100 STBL in a spectrum of low-level temperature advection ranging from the extremely cold air
101 advection such as cold air outbreaks to the warm air advection in the warm sector of mid-latitude
102 cyclones. The STBLs embedded in cold air advection flows are either fully coupled (i.e. well-
103 mixed) or Cu-coupled. The unambiguously decoupled STBLs only occur in warm air advection
104 conditions where the stable stratification is sufficiently strong to prohibit the cumulus coupling.
105 This view is supported by ground-based observations from the Southern Ocean, northeast
106 subtropical Pacific, and northeast Atlantic. These observations show that, as the low-level flow

shifts from cold to warm air advection, the boundary layer turns from a Cu-coupled STBL to a considerably stably stratified STBL without Cu coupling (i.e. unambiguously decoupled STBL).

Poorly understood is the unambiguously decoupled STBLs experiencing warm advection. In contrast to Cu-coupled STBLs, typical at subtropics, the STBLs under warm advection conditions receive scarce attention despite their potential abundance in midlatitudes (Agee, 1987; Fletcher et al., 2016; Wall et al., 2017; Scott et al., 2020). This motivates the current study. We aim to elucidate the physics of STBL response to warm advection using idealized large-eddy simulations. By the "idealized", we mean simulating an STBL over a doubly periodic domain with the sea surface temperature (SST) decreasing over time to mimic the influences of warm air advection. This idealized setup is the same as the conventional LES studies of Sc-to-Cu transitions (Sandu and Stevens, 2011; Van der Dussen et al., 2013; Bretherton and Blossey, 2014), in which the SST increases over time. Such consistency allows for direct comparisons.

In addition to further the understanding of decoupling dynamics, another motivation is a lack of consensus on the role of horizontal temperature advection on low cloud radiative effects. Prior observations show that marine low clouds are considerably fewer and thinner under warmer air advection conditions (Norris and Iacobellis, 2005; Myers and Norris, 2015; Klein et al., 2017; Scott et al., 2020). Their interpretation is that the warm-advection-induced decoupling leads to less moisture supply from the sea surface to the clouds, thereby thinning the clouds. Contrasting pieces of evidence, however, exist. For example, Zheng and Li (2019) found that clouds can be very persistent even if they are decoupled from the sea surface under warm advection conditions, as shown by geostationary satellite images and ship-based remote sensing data. This finding is consistent with Goren et al. (2018b) who found that precipitating marine clouds are more persistent in decoupled STBLs than coupled ones. Moreover, some studies show

no statistically significant dependence of low cloud radiative effects on temperature advection in climate models (personal communications with Daniel McCoy) and ground-based observations over mid-latitude oceans (Naud et al., 2020). The mixed lines of evidence suggest a lack of understanding of the mechanism underlying the low cloud response to warm air advection.

In summary, this study attempts to elucidate the physical mechanisms of warm-advection-induced decoupling (part 1) and its control on low-cloud radiative effects (part 2) by using idealized large-eddy simulations. Part 1 is dedicated to decoupling dynamics whereas part 2 focuses on its implications for the low cloud feedback. Although the warm air advection is our focus, our analyses are centered on comparing the results of warm air advection with the cold air advection (as the benchmark). This enables a clearer presentation of the new insights in the context of conventional knowledge. The next section introduces the LES model and the experiments. Section 3 shows the results, followed by discussions and concluding remarks.

2. Large-Eddy Simulations

2.1. Model and case descriptions

We use the System for Atmospheric Modeling (SAM) model, version 6.11.3 (Khairoutdinov and Randall, 2003). SAM uses liquid water static energy (h_l), total non-precipitating water mixing ratio (q_t), and total precipitating water mixing ratio as prognostic thermodynamic scalars. We use the advection scheme developed by Smolarkiewicz and Grabowski (1990), a simplified (drizzle only) version of Khairoutdinov and Kogan (2000)'s microphysics scheme and RRTMG radiation (Iacono et al., 2008). Surface fluxes of temperature, moisture, and momentum are calculated by similarity theory.

We use a horizontal grid spacing of 35 m in a doubly periodic domain with a size of 4480^2 m^2. We chose such a small domain size purely for computational efficiency. It should be too small to represent mesoscale convective circulation typical for precipitating STBLs. The STBLs studied here are weakly precipitating so that the influence of mesoscale dynamics should be minor. This is confirmed by a sensitivity test for a larger domain of 8960^2 m^2 that yields nearly identical results (not shown). The vertical grid spacing is set as 5 m in the cloud and inversion layer to resolve entrainment. The grid spacing stretches above ~ 2400 m until the domain top of ~ 4200 m, which is high enough for gravity wave damping. There is a total of 512 vertical grids.

The base case for our simulations is the case from the Atlantic Stratocumulus Transition Experiment (ASTEX) (Albrecht et al., 1995). The ASTEX case has been a benchmark for LES simulations of the Sc-to-Cu transitions (Van der Dussen et al., 2013). A unique aspect of the ASTEX case is that observations from an aircraft and balloons are "Lagrangian" for they follow the evolution of STBL air mass. This is particularly important for simulating the STBL response to horizontal temperature advection, for which the SST evolution along the air mass trajectory is the key driver. During the ASTEX, the SST increases by ~ 4 K over the 40-hour simulation of the ASTEX case. Such an increase in SST is widely regarded as the determinant driver of the cloud regime transition.

As stated in the introduction, we use a cold air advection case as a benchmark for understanding the role of warm advection. To that end, we conduct two idealized experiments by simplifying the forcing of the original ASTEX case. In the first experiment, we linearize the SST increase rate, yielding an SST increasing rate of 2.6 K/day (named "CADV"). In the second experiment, we decrease the SST by 2.6 K/day to mimic the influence of warm air advection

174 (named "WADV"). All other initial and forcing conditions are the same (see Van der Dussen et
175 al., 2013 for the detail).

176 The WADV run is highly idealized. In the real world, the low-level horizontal temperature
177 advection strongly couples with other synoptic variables. For example, warm air advection
178 typically co-occurs with large-scale ascent motions whereas cold air advection is more likely to
179 occur in a subsiding atmosphere (Holton, 1973; Norris and Klein, 2000; Zheng et al., 2020). In
180 that regard, it is unrealistic that the CADV and WADV experience the same large-scale forcing.
181 But, the purpose of this study is not to reproduce the real-world STBLs, but to understand the
182 most essential physics behind the problem. All the existing hypotheses for STBL response to
183 warm air advection are centered on the stabilization effect of warm advection as the most
184 determinant process (Norris and Iacobellis, 2005; Klein et al., 2017; Scott et al., 2020). In other
185 words, our current level of understanding does not allow for formulating a hypothesis
186 sophisticated enough to account for every aspect of the problem. Thus, we consider our
187 simulations a starting point for future more realistic numerical explorations.

188 2.2. Diagnostic statistics

189 The boundary layer height (z_i) and heights of capping inversion base and top are
190 determined using the method developed by Yamaguchi and Randall (2011) that is based on the
191 geometry of h_l variance. This allows us to compute the buoyancy jump across the inversion,
192 which will be used to quantify the entrainment-driven decoupling shown later. We quantify the
193 degree of stratification of an STBL using the h_l averaged over the top 10% of the z_i minus the h_l
194 averaged over the bottom 10% of the z_i, marked as $\Delta_{BL}h_l$.

We determine the lifting condensation level (LCL) using the exact analytic formula developed by Romps (2017). The entrainment rate (w_e) is determined using the boundary layer mass budget equation: $w_e = dz_i/dt - w_{sub}$, in which the w_{sub} is the large-scale subsidence rate at the boundary layer top.

3. Results

3.1. Time evolution

Figures 2 and 3 show the time evolution of selected outputs, which illustrate many characteristics of the STBL under the influence of warm air advection. The warm air advection substantially suppresses the surface latent and sensible heat fluxes (Figs. 2a and b). This lowers the turbulence level of the boundary layer, weakens the entrainment near the boundary layer top (Fig. 2d), and slows the deepening (or even shallowing) of the boundary layer (Fig. 2c). Such a contrast in surface fluxes, as will be evident later, is the most essential factor explaining most of the differences between the two simulations.

Figures 3a and b show the time-height plots of the cloud fraction for the two runs. The CADV presents a textbook-like Sc-to-Cu transition whereas the WADV shows a solid Sc deck persistent throughout the simulation. The persistence is primarily due to the weak entrainment drying, discussed in detail in part 2 (Zhang et al., 2021). Because the focus of this study is the boundary layer decoupling, we look at time evolution of h_l and q_t profiles (Figures 3 c-f). Both regimes show increasingly stably stratified boundary layers, but their geometries of stratification differ greatly, which can be more clearly seen from the sounding at a selected time of t = 30 h (Fig. 4). In CADV, the boundary layer is stratified into two well-mixed layers: the upper cloud-

containing layer driven by radiative cooling and the bottom layer driven by surface heating. These two layers are separated by a weakly stratified layer. In WADV, however, the stratification concentrates near the surface, as seen from a well-defined temperature inversion in the lowest quarter of the boundary layer. Above the inversion is a well-mixed cloud-containing layer. The convection in this mixed-layer is driven by cloud-top radiative cooling, suggested by the top-heavy structure of vertical velocity variance (Fig. 3h and Fig. 4c) and the negative vertical velocity skewness (Fig. 3j), an indicator of top-driven convection (Moeng and Rotunno, 1990).

The above analysis dictates two different decoupling mechanisms: entrainment-warming-driven decoupling in CADV and surface-cooling-driven decoupling in WADV. This statement can be demonstrated by quantifying the role of entrainment warming in decoupling. Here we use a model diagnostic called "excess entrainment warming" (EEW), developed by Zheng et al. (2021). The EEW is defined as:

$$EEW = \underbrace{\rho C_p w_e \Delta_{inv} \theta_v}_{Entrainment\ warming} + \underbrace{\Delta_{cld} F_{rad} + \rho L_v \Delta_{cld} F_{prec}}_{Diabatic\ cooling}, \quad (1)$$

where ρ is the air density, C_p is the specific heat of air, L_v is the latent heat of evaporation of water, F_{rad} is the radiative flux (W m^{-2}), and F_{prec} is the precipitation flux (m^{-1}). The symbol "Δ_{cld}" represents the divergence across the Sc cloud layer. A larger EEW means that the diabatic cooling (radiative cooling compromised by precipitation-induced heating) is not sufficient to balance the entrainment warming so that the entrained air is not cold enough to be sink through the sub-cloud layer. This causes the accumulation of warm air in the upper boundary layer, stably stratifying the STBL. A small or even negative value means that the entrainment-induced warming is balanced by the diabatic cooling, preventing the decoupling. Figure 2g shows the

239 evolution of EEW for the two experiments. The CADV has an EEW of several tens of W m^{-2}
240 throughout the two simulations, suggesting that entrainment warming considerably outweighs
241 the diabatic cooling. On the contrary, the EEW remains negative most of the time in WADV,
242 demonstrating a minimal role of entrainment in the decoupling.

243 Given that the entrainment cannot explain the decoupling in WADV, the near-surface
244 cooling is the dominant decoupling factor. To understand what drives the near-surface cooling in
245 WADV, we analyze the budgets of $\frac{dh_l}{dt}$ in the lowest 200 m when the cooling is most distinctive.
246 We found that the turbulent transport, $(\frac{dh_l}{dt})_{tur}$, and radiation, $(\frac{dh_l}{dt})_{rad}$, are the dominant
247 controllers, which can be illustrated in Figure 5. The cooling effect of turbulent transport is
248 straightforward to understand. In WADV, except at the beginning, boundary layer air is notably
249 warmer than the SST (Fig. 2g), leading to the downward loss of heat to the sea surface. This
250 causes cooling of the bottom boundary layer. However, turbulent transport is not the only
251 cooling mechanism, as seen from the thin layer of turbulent warming in the lowest few tens of
252 meters (Fig. 5b).

253 The thin layer of turbulent warming can be explained by the turbulence adjustment to the
254 near-surface radiative cooling (Fig. 5c). What causes the abnormally large radiative cooling near
255 the surface? According to the conventional knowledge about radiative transfer, we know that
256 atmospheric radiative cooling has three contributing components: (1) exchange of radiative
257 energy with underlying atmosphere, (2) exchange of radiative energy with overlying atmosphere,
258 and (3) radiative energy escaping to the cold space. In a typical atmosphere where temperature
259 decreases with altitude, the first two components roughly cancel each other, leaving the
260 "cooling-to-space" component the dominant one (Petty, 2006). This is not the case here for the

air near the surface: both the overlying and underlying airs are cooler (Fig. 4a). Thus, exchanges of radiative energy in both directions cause loss of energy, considerably increasing the radiative cooling. Such a local cooling induces local convergence of turbulent flux as an adjustment process.

The aggregate role of the radiation and turbulence, $(\frac{dh_l}{dt})_{tur+rad}$, is a cooling effect. The $(\frac{dh_l}{dt})_{tur+rad}$ (Fig. 5d) bears a similarity with the $\frac{dh_l}{dt}$ (Fig. 5a), suggesting that the two processes can explain the bulk of the near-surface cooling. The remaining difference is due to the precipitation and large-scale transport, which play a secondary role.

In summary, the stable stratifications of STBLs in CADV and WADV are explained by entrainment-induced warming and near-surface cooling (by turbulence and radiation), respectively. These two decoupling mechanisms can be conceptualized into a decoupling dipole: top-warming-driven versus bottom-cooling-driven decoupling.

3.2. The already decoupled phase

We have discussed processes leading to the decoupling in both regimes. Now we characterize the turbulent properties of STBLs in their already decoupled phases. Strictly speaking, there is no such thing as an equilibrium phase in our simulations because the SST keeps evolving and the STBL keeps responding. Here, we take model outputs at t = 30 h as representations of already decoupled STBLs for the two regimes. One justification for selecting t = 30 h is that the stratification degree at CADV already saturates at t = 30 h, suggesting a quasi-equilibrium state (Fig. 2e). In WADV, the STBL is still stratifying, but the qualitative

282 characteristics of the STBL (e.g. thermodynamic structure, turbulence, and cloud properties)
283 remain similar throughout the simulations. Selecting different times of the WADV run does not
284 influence the main conclusion of this paper.

285 We first look at the three-dimensional (3D) visualization of the STBLs at t = 30 h (Figure
286 6). To more clearly visualize the cloud-surface decoupling, we show the surface plots of the
287 near-surface q_t, defined as the top 1% of q_t in the vertical (dark red surface). The CADV regime
288 is characterized by intermittent Cu clouds penetrating the Sc deck, known as the Cu-coupled
289 STBL. The contour of the near-surface q_t extends vertically from the surface to the base of Cu.
290 Through the conduit of Cu, the water from the sea surface feeds into the Sc deck. Such a feeding
291 effect is absent in WADV. In WADV, there is only a single layer of solid Sc deck, completely
292 separate from the surface humid air trapped near the surface. We provide movies of 2-D fluid
293 visualization for the two runs to aid in intuitively understanding the results (see Animations 1
294 and 2 in the supplemental material).

295 Such a difference in the cloud-surface interaction is augmented by vertical velocity fields
296 at different levels. Figure 7 shows the vertical velocity at z = 10 m (left), z = 0.5z_b (middle), and
297 z = z_b (right). The turbulent flow near the surface of the CADV regime is elongated, consistent
298 with the typical flow structure in convective boundary layers (Moeng and Rotunno, 1990). In
299 WADV, however, the flow is more random with a less evident elongated pattern, typical for
300 stratified flows (Mahrt, 2014). At z = 0.5z_b in the CADV, small patches of isolated updrafts
301 (blobs of red colors) start to emerge. These updraft regions are more humid than the surrounding
302 regions. This pattern resembles the typical "cumulus-like" convection: moist, narrow, and strong
303 updrafts surrounded by drier, wider, and weaker subsidence (Bjerknes, 1938). This is further
304 supported by the positive skewness of vertical velocity, characteristic of surface-driven

convection (Figure 7h). In WADV, however, the "cumulus-like" convection is absent, as seen from a lack of concentrated updrafts. The skewness of vertical velocity is negative (Figure 7h), suggesting a dominance of top-cooling-driven turbulence (Wyngaard, 1987; Moeng and Rotunno, 1990). Such a contrast in turbulence regime persists at $z = z_b$.

The flow visualizations (Figs 6 and 7) suggest two distinctive convection regimes: surface-heating-driven cumulus-like convection for CADV versus top-cooling-driven stratocumulus-like convection for WADV. Such a difference can be more directly seen by conditionally sampling the parcels in rising ($w > 0$) and sinking motions ($w < 0$) (Fig. 8a). Fig. 8a shows that the vertical velocity variance is considerably stronger for updrafts than downdrafts in CADV, suggesting a more determinant role of updrafts in driving the vertical mixing, whereas the opposite is true for WADV. Note that the cloud-top radiative cooling still contributes to driving the convection in the CADV, as seen from the local maxima of vertical velocity variance in the upper Sc layer. But even in such a Sc layer, the updrafts contribute more to the turbulence via penetration of the Cu convection.

The relative strength of updrafts and downdrafts makes a substantial difference to how heat and moisture are transported in the vertical (Figs. 8b,c). In CADV, the vertical transport of moisture is realized by updrafts that carry humidity from the sea surface upward, feeding the Sc deck (Fig. 8b). In contrast, in the WADV, the downdrafts play a more dominant role in the vertical exchange of moisture: downdrafts transport entrained dry air toward the surface. At $z = z_b$ of WADV, the supply of moisture via updrafts is close to zero, suggesting that the Sc deck almost entirely decouples from the source of humidity from below.

A similar conclusion can be drawn from the heat flux (Fig. 8c). The heat flux profile is relatively more complex due to the influences of diabatic heating/cooling (i.e. radiation and precipitation) to which the turbulent flux must adjust (Stevens et al., 1998). Hence we focus on the sub-cloud layer where the diabatic heating/cooling is minimal. Both regimes show a downward transport of heat, but the transport in CADV is realized by updrafts, whereas, in WADV, the downdrafts drive the downward transports of warm entrained air.

In addition to the profiles of heat and moisture fluxes, it is informative to look at the buoyancy flux that dictates boundary layer energetics (Fig. 8d). In CADV, the buoyancy flux is mostly positive except near the LCL. Such a structure of buoyancy profile is consistent with the conventional wisdom based on the argument of hypothetical parcel trajectory (see Bretherton et al., 1997 for detail). Again, the updrafts dominate the positive buoyant flux (light air rises), converting the potential energy of the environment to turbulent kinetic energy. Such a large buoyancy for updrafts is largely contributed by the water vapor. As seen in Fig. 8c, the heat flux for updrafts is negative throughout most of the boundary layer, which suggests cooler air ascending. The buoyancy of the ascending cool air stems from the water vapor, as seen from the strong q_t flux in updrafts (Fig. 8b). In WADV, however, the cloud-layer and sub-cloud layer exhibit opposite signs. In the cloud-layer, the buoyancy flux is positive, contributed by both updrafts and downdrafts through latent heating and diabatic cooling, respectively. The downdrafts, again, contribute more. In the sub-cloud layer, the buoyancy flux is slightly negative. Such a dipole-like geometry of buoyancy flux profile resembles that of the heat flux (Fig. 8c), suggesting the contribution of buoyancy from water vapor is insignificant, especially in the sub-cloud layer.

So what drives the donward motion of the warm air if the water vapor effect does not contribute? From the perspective of the heat budget constraint, the warm air must descend somewhere in the sub-cloud layer in order to transfer heat from the atmosphere into the sea surface, a necessary consequence of WADV (warm air overlying cold surface). Then, what are the underlying mechanisms? We explain it using the argument from Schubert et al. (1979a) who stress the role of the pressure field. The central idea is that the pressure gradient force propels the air overturning, which overcomes the negative buoyancy. This effect can be more clearly illustrated by the $\overline{w'p'}$ profile of the WADV experiment (Fig. 9). The $\overline{w'p'}$ is negative in the sub-cloud layer for both updrafts and downdrafts. This suggests that air rises in low-pressure regions and sinks in high-pressure regions, typical for pressure-driven air overturning. The negative $\overline{w'p'}$ at the cloud base suggests that the cloud layer does work to the sub-cloud layer, pumping up the sub-cloud air, completing the circulation. This process is consistent with the idea of boundary layer energetics. As the boundary layer being stabilized by the warm air advection, the turbulence generated from the cloud-top radiative cooling must work against the stability to well mix the boundary layer. This is a process that converts turbulent energy to the potential energy of the environment. Such an energy conversion is realized by the descending of warm air, propelled by the pressure gradient.

3.3. On the formation of double-layer stratiform clouds

From observations, under warm air advection conditions, often found are double-layer stratiform clouds, with the upper layer capped by the major temperature inversion and the lower layer close to the surface, often manifested as fog (Zheng et al., 2020) (personal communications

370 with Mark Smalley and Steven Klein). Such a double-layer cloud regime is distinctive from the
371 Cu-fed Sc because the lower clouds are stratiform, not cumuliform. It is, thus, important to
372 understand why our WADV experiment does not develop a stratus near surface.

373 A hypothesis that naturally arises is that, in the WADV run, the near-surface temperature
374 inversion is not sufficiently strong to sustain high humidity (by trapping water vapor within it).
375 To test this hypothesis, we run additional simulations by altering the forcing parameters for the
376 WADV. First, we double the Tadv from 2.6 K/day to 5.2 K/day, denoted as "WADV5.2". The
377 expectation is that if the SST cools rapidly enough, the near-surface inversion may be strong
378 enough to form fogs. Second, we decrease the large-scale divergence from $5*10^{-6}$ to $3*10^{-6}$,
379 denoted as "WADV Div3". We expect that, for weaker subsidence, the boundary layer deepens
380 more rapidly, enhancing the warming of the upper boundary layer, which strengthens the near-
381 surface temperature inversion.

382 Figure 10 shows the cross-sections of cloudiness of the two experiments. A double-layer
383 stratiform cloud emerges in the WADV Div3, but not in WADV5.2 (only a tiny amount of small
384 clouds below the Sc deck). The bottom panel of Fig. 10 shows the sounding at t = 30 h. The
385 filled circles mark the heights of the near-surface temperature inversion, z_{li}, determined as the
386 level of the local maxima of liquid water potential temperature variance (Yamaguchi and Randall,
387 2008). We find that both new experiments generate stronger near-surface inversions than the
388 WADV (Fig. 10c), consistent with our expectations. However, a strong temperature inversion
389 does not necessarily increase the q_t: relative to WADV, the q_t within the inversion is higher in
390 WADV Div3, but lower in WADV5.2 (Fig. 10d). For this reason, the WADV5.2 does not
391 develop enough high RH to form a cloud (Fig. 10e).

To understand what drives the difference in the q_t, we consider the atmosphere from the surface to the z_{li} as a bulk layer and take the $\overline{w'q_t'}$ at the top and bottom, denoted as $(\overline{w'q_t'})_{top}$ and $(\overline{w'q_t'})_{bot}$, respectively (Fig. 11a and b). Their difference divided by the z_{li} yields the net moistening rate of the near-surface layer (Fig. 11c). We found considerably smaller $(\overline{w'q_t'})_{bot}$ in WADV5.2 than the other two runs (Fig. 11b), suggesting that the downward loss of humidity is the primary reason for its greater drying (Fig. 11c and Fig. 10d). The negative $(\overline{w'q_t'})_{bot}$ is driven by the more negative q_t gradient across the surface, namely q_{sfc}^* - q_{air}, where the q_{sfc}^* is the saturation q_t of the SST and q_{air} is the q_t of the overlying air (Fig. 11d). The more negative q_{sfc}^* - q_{air} is fundamentally constrained by the Clausiou-Clapeyron relationship. Unlike the WADV5.2, the WADV Div 3 does not experience any changes in the $(\overline{w'q_t'})_{bot}$ compared with the WADV. Instead, the $(\overline{w'q_t'})_{top}$ becomes markedly smaller than that of the WADV[1]. This means less upward loss of moisture, thereby elevating the q_t relative to the WADV.

In summary, weaker subsidence favors the emergence of double-layer stratiform clouds because weaker subsidence allows for more rapid boundary layer deepening, which warms the upper boundary layer, enhancing the temperature inversion in the lower boundary layer. The stronger temperature inversion traps the moisture within, eventually elevating the RH to unity. Stronger warm advection (i.e. more rapid sea surface cooling) does not necessarily favor the formation of such secondary stratus because a cooler sea surface facilitates the downward transport of moisture from the atmosphere into the sea. This acts to dry the near-surface air, preventing the formation of clouds.

[1] The smaller $(\overline{w'q_t'})_{top}$ is driven by the stronger near-surface temperature inversion at WADV Div3 (Fig. 10a), which inhibits the vertical exchange of moisture between the bottom and upper boundary layer.

4. Summary

We have investigated the response of a stratocumulus-topped boundary layer (STBL) to a cooling sea surface by using idealized large-eddy simulations. The decreasing sea surface temperature mimics the influence of low-level warm air advection (WADV). In addition to characterizing the basic turbulence structure of the boundary layer in WADV, we are particularly interested in testing an unproven argument: an unambiguous decoupling between stratocumulus clouds and the surface can be achieved in warm air advection (WADV) flow, but not in cold advection (CADV) flow because the latter favors cumulus-induced coupling while the former doesn't (Zheng and Li, 2019; Zheng et al., 2020). To examine this argument, we investigate the decoupling physics of an STBL experiencing WADV and compare the results with that in CADV. We found the followings:

i. An STBL tends to become stably stratified in both WADV and CADV conditions, but their driving mechanism is dramatically different. The stratification in CADV is caused by the enhanced entrainment warming (i.e. the "deepening-warming" theory by Bretherton and Wyant, 1997) whereas, in WADV, it is driven by cooling of the bottom boundary layer due to radiative cooling and loss of heat to the sea surface via turbulent transport. The difference in the driving mechanism constitutes a decoupling dipole: top-warming-driven versus bottom-cooling-driven.

ii. The surface cooling in the WADV causes a temperature inversion in the lower boundary layer. Above the inversion is a well-mixed cloud-containing layer whose convection is driven by the cloud-top radiative cooling. This is different from the

435 temperature structure in CADV that has two well-mixed layers separated by a
436 conditionally unstable layer.
437
438 iii. The difference in the boundary layer thermodynamics between WADV and CADV
439 significantly alters the turbulence and cloud regimes. Unlike the emergence of
440 cumulus-coupled stratocumulus in CADV, the WADV simulation manifests a
441 single stratocumulus deck that is persistent, horizontally homogeneous, relatively
442 quiet, and unambiguously decoupled from the moisture source of the sea surface.
443 Such a cloud pattern is a consequence of a lack of surface fluxes, leaving the cloud-
444 top cooling the only driver of convection.
445
446 iv. Due to the lack of surface fluxes, the buoyancy flux profile in WADV manifests a
447 dipole pattern: positive in the cloud layer and weakly negative in the sub-cloud
448 layer. This, in combination with the profile of the pressure covariation with the
449 vertical velocity, dictates that the cloud layer does work to the sub-cloud layer to
450 pump up the air, maintaining the convective circulation. Such a cloud-containing
451 mixed-layer, however, cannot extend down to the surface because of the strong
452 near-surface inversion sustained by the surface cooling. This is, again, in contrast to
453 the convective circulation in CADV that is not only driven by cloud-top cooling but
454 also surface heating that propels strong updrafts responsible for the bulk of the heat
455 and moisture transports.
456

v. A secondary stratiform cloud (or fog) can form in the lower boundary layer in WADV if the large-scale subsidence weakens. The mechanism is that the STBL deepens more rapidly if the subsidence is weaker. This leads to more effective entrainment near the STBL top, warming the boundary layer and enhancing the temperature gradient between the warm boundary layer and the cold surface. This strengthens the near-surface temperature inversion, trapping more water vapor within the layer, raising the relative humidity to unity. Interestingly, increasing the cooling rate of sea surface temperature does not necessarily cause the formation of the fog. The reason is that colder sea surface enhances the negative moisture gradient between the air in contact with the sea surface and the overlying air. This causes a more rapid loss of moisture from the near-surface air to the sea, thereby suppressing the fog formation.

Acknowledgments

This study is supported by the Department of Energy (DOE) Atmospheric System Research program (DE-SC0018996). S. S. Lee is also supported by the National Research Foundation of Korea (NRF) grant funded by the South Korean government (MSIT) (grant no. NRF2020R1A2C1003215). The SAM model code is available at http://rossby.msrc.sunysb.edu/~marat/SAM.html. We thank Marat Khairoutdinov for maintaining the SAM code and Peter Blossey for helping with setting up the ASTEX case.

478 **Reference:**

479 Agee, E. M. (1987). Mesoscale cellular convection over the oceans. *Dynamics of atmospheres*
480 *and oceans, 10*(4), 317-341.

481 Albrecht, B. A., Bretherton, C. S., Johnson, D., Schubert, W. H., & Frisch, A. S. (1995). The
482 Atlantic stratocumulus transition experiment—ASTEX. *Bulletin of the American*
483 *Meteorological Society, 76*(6), 889-904.

484 Bretherton, C. S., & Blossey, P. N. (2014). Low cloud reduction in a greenhouse□warmed
485 climate: Results from Lagrangian LES of a subtropical marine cloudiness transition.
486 *Journal of Advances in Modeling Earth Systems, 6*(1), 91-114.

487 Bretherton, C. S., Uchida, J., & Blossey, P. N. (2010). Slow manifolds and multiple equilibria in
488 stratocumulus□capped boundary layers. *Journal of Advances in Modeling Earth Systems,*
489 *2*(4).

490 Bretherton, C. S., & Wyant, M. C. (1997). Moisture transport, lower-tropospheric stability, and
491 decoupling of cloud-topped boundary layers. *Journal of the Atmospheric Sciences, 54*(1),
492 148-167.

493 Caldwell, P., & Bretherton, C. S. (2009). Response of a subtropical stratocumulus-capped mixed
494 layer to climate and aerosol changes. *Journal of Climate, 22*(1), 20-38.

495 Caldwell, P., Bretherton, C. S., & Wood, R. (2005). Mixed-layer budget analysis of the diurnal
496 cycle of entrainment in southeast Pacific stratocumulus. *Journal of the Atmospheric*
497 *Sciences, 62*(10), 3775-3791.

498 Fletcher, J. K., Mason, S., & Jakob, C. (2016). A climatology of clouds in marine cold air
499 outbreaks in both hemispheres. *Journal of Climate, 29*(18), 6677-6692.

500 Goren, T., Rosenfeld, D., Sourdeval, O., & Quaas, J. (2018a). Satellite Observations of
501 Precipitating Marine Stratocumulus Show Greater Cloud Fraction for Decoupled Clouds
502 in Comparison to Coupled Clouds. *Geophysical Research Letters, 0*(0).
503 https://agupubs.onlinelibrary.wiley.com/doi/abs/10.1029/2018GL078122
504 Goren, T., Rosenfeld, D., Sourdeval, O., & Quaas, J. (2018b). Satellite observations of
505 precipitating marine stratocumulus show greater cloud fraction for decoupled clouds in
506 comparison to coupled clouds. *Geophysical Research Letters*.
507 Hahn, C. J., & Warren, S. G. (2007). *A gridded climatology of clouds over land (1971-96) and*
508 *ocean (1954-97) from surface observations worldwide*.
509 Hartmann, D. L., Ockert-Bell, M. E., & Michelsen, M. L. (1992). The effect of cloud type on
510 Earth's energy balance: Global analysis. *Journal of Climate, 5*(11), 1281-1304.
511 Holton, J. R. (1973). An introduction to dynamic meteorology. *American Journal of Physics,*
512 *41*(5), 752-754.
513 Iacono, M. J., Delamere, J. S., Mlawer, E. J., Shephard, M. W., Clough, S. A., & Collins, W. D.
514 (2008). Radiative forcing by long□lived greenhouse gases: Calculations with the AER
515 radiative transfer models. *Journal of Geophysical Research: Atmospheres, 113*(D13).
516 Jones, C., Bretherton, C., & Blossey, P. (2014). Fast stratocumulus time scale in mixed layer
517 model and large eddy simulation. *Journal of Advances in Modeling Earth Systems, 6*(1),
518 206-222.
519 Khairoutdinov, M., & Kogan, Y. (2000). A new cloud physics parameterization in a large-eddy
520 simulation model of marine stratocumulus. *Monthly Weather Review, 128*(1), 229-243.

Khairoutdinov, M. F., & Randall, D. A. (2003). Cloud resolving modeling of the ARM summer 1997 IOP: Model formulation, results, uncertainties, and sensitivities. *Journal of the Atmospheric Sciences, 60*(4), 607-625.

Klein, S. A., Hall, A., Norris, J. R., & Pincus, R. (2017). Low-cloud feedbacks from cloud-controlling factors: a review. In *Shallow Clouds, Water Vapor, Circulation, and Climate Sensitivity* (pp. 135-157): Springer.

Lilly, D. K. (1968). Models of cloud□topped mixed layers under a strong inversion. *Quarterly Journal of the Royal Meteorological Society, 94*(401), 292-309.

Mahrt, L. (2014). Stably stratified atmospheric boundary layers. *Annual Review of Fluid Mechanics, 46*, 23-45.

Miller, M. A., & Albrecht, B. A. (1995). Surface-based observations of mesoscale cumulus–stratocumulus interaction during ASTEX. *Journal of the Atmospheric Sciences, 52*(16), 2809-2826.

Moeng, C.-H., & Rotunno, R. (1990). Vertical-velocity skewness in the buoyancy-driven boundary layer. *Journal of the Atmospheric Sciences, 47*(9), 1149-1162.

Myers, T. A., & Norris, J. R. (2015). On the relationships between subtropical clouds and meteorology in observations and CMIP3 and CMIP5 models. *Journal of Climate, 28*(8), 2945-2967.

Naud, C.M., Booth, J.F., Protat, A., Lamer, K., Marchand, R. and McFarquhar, G.M., Boundary Layer Cloud Controlling Factors in the Midlatitudes: Southern versus Northern Ocean Clouds. In *AGU Fall Meeting 2020*. AGU.

Nicholls, S. (1984). The dynamics of stratocumulus: Aircraft observations and comparisons with a mixed layer model. *Quarterly Journal of the Royal Meteorological Society, 110*(466), 783-820.

Nicholls, S., & Leighton, J. (1986). An observational study of the structure of stratiform cloud sheets: Part I. Structure. *Quarterly Journal of the Royal Meteorological Society, 112*(472), 431-460.

Norris, J. R., & Iacobellis, S. F. (2005). North Pacific cloud feedbacks inferred from synoptic-scale dynamic and thermodynamic relationships. *Journal of Climate, 18*(22), 4862-4878.

Norris, J. R., & Klein, S. A. (2000). Low cloud type over the ocean from surface observations. Part III: Relationship to vertical motion and the regional surface synoptic environment. *Journal of Climate, 13*(1), 245-256.

Petty, G. W. (2006). *A first course in atmospheric radiation*: Sundog Pub.

Romps, D. M. (2017). Exact Expression for the Lifting Condensation Level. *Journal of the Atmospheric Sciences, 74*(12), 3891-3900.

Sandu, I., & Stevens, B. (2011). On the factors modulating the stratocumulus to cumulus transitions. *Journal of the Atmospheric Sciences, 68*(9), 1865-1881.

Schubert, W. H., Wakefield, J. S., Steiner, E. J., & Cox, S. K. (1979a). Marine stratocumulus convection. Part I: Governing equations and horizontally homogeneous solutions. *Journal of the Atmospheric Sciences, 36*(7), 1286-1307.

Schubert, W. H., Wakefield, J. S., Steiner, E. J., & Cox, S. K. (1979b). Marine stratocumulus convection. Part II: Horizontally inhomogeneous solutions. *Journal of Atmospheric Sciences, 36*(7), 1308-1324.

564 Scott, R. C., Myers, T. A., Norris, J. R., Zelinka, M. D., Klein, S. A., Sun, M., & Doelling, D. R.
565 (2020). Observed Sensitivity of Low Cloud Radiative Effects to Meteorological
566 Perturbations over the Global Oceans. *Journal of Climate*.
567 Smolarkiewicz, P. K., & Grabowski, W. W. (1990). The multidimensional positive definite
568 advection transport algorithm: Nonoscillatory option. *Journal of Computational Physics,*
569 *86*(2), 355-375.
570 Stevens, B. (2006). Bulk boundary-layer concepts for simplified models of tropical dynamics.
571 *Theoretical and Computational Fluid Dynamics, 20*(5-6), 279-304.
572 Stevens, B., Cotton, W. R., Feingold, G., & Moeng, C.-H. (1998). Large-eddy simulations of
573 strongly precipitating, shallow, stratocumulus-topped boundary layers. *Journal of the*
574 *Atmospheric Sciences, 55*(24), 3616-3638.
575 Uchida, J., Bretherton, C., & Blossey, P. (2010). The sensitivity of stratocumulus-capped mixed
576 layers to cloud droplet concentration: Do LES and mixed-layer models agree?
577 *Atmospheric Chemistry and Physics, 10*(9), 4097-4109.
578 Van der Dussen, J., De Roode, S., Ackerman, A. S., Blossey, P. N., Bretherton, C. S., Kurowski,
579 M. J., et al. (2013). The GASS/EUCLIPSE model intercomparison of the stratocumulus
580 transition as observed during ASTEX: LES results. *Journal of Advances in Modeling*
581 *Earth Systems, 5*(3), 483-499.
582 Wakefield, J. S., & Schubert, W. H. (1981). Mixed-layer mode simulation of eastern North
583 Pacific stratocumulus. *Monthly Weather Review, 109*(9), 1952-1968.
584 Wall, C. J., Hartmann, D. L., & Ma, P.-L. (2017). Instantaneous linkages between clouds and
585 large-scale meteorology over the Southern Ocean in observations and a climate model.
586 *Journal of Climate, 30*(23), 9455-9474.

587 Wood, R. (2007). Cancellation of aerosol indirect effects in marine stratocumulus through cloud
588 thinning. *Journal of the Atmospheric Sciences, 64*(7), 2657-2669.
589 Wood, R. (2012). Stratocumulus clouds. *Monthly Weather Review, 140*(8), 2373-2423.
590 Wyngaard, J. (1987). A physical mechanism for the asymmetry in top-down and bottom-up
591 diffusion. *Journal of the Atmospheric Sciences, 44*(7), 1083-1087.
592 Yamaguchi, T., & Randall, D. A. (2008). Large-eddy simulation of evaporatively driven
593 entrainment in cloud-topped mixed layers. *Journal of the Atmospheric Sciences, 65*(5),
594 1481-1504.
595 Zhang, Y., Stevens, B., & Ghil, M. (2005). On the diurnal cycle and susceptibility to aerosol
596 concentration in a stratocumulus□topped mixed layer. *Quarterly Journal of the Royal*
597 *Meteorological Society: A journal of the atmospheric sciences, applied meteorology and*
598 *physical oceanography, 131*(608), 1567-1583.
599 Zheng, Y., & Li, Z. (2019). Episodes of Warm□Air Advection Causing Cloud□Surface
600 Decoupling During the MARCUS. *Journal of Geophysical Research: Atmospheres*.
601 Zheng, Y., Rosenfeld, D., & Li, Z. (2018). The Relationships Between Cloud Top Radiative
602 Cooling Rates, Surface Latent Heat Fluxes, and Cloud□Base Heights in Marine
603 Stratocumulus. *Journal of Geophysical Research: Atmospheres, 123*(20), 11,678-611,690.
604 Zheng, Y., Rosenfeld, D., & Li, Z. (2020). A More General Paradigm for Understanding the
605 Decoupling of Stratocumulus□Topped Boundary Layers: The Importance of Horizontal
606 Temperature Advection. *Geophysical Research Letters, 47*(14), e2020GL087697.
607 Zheng, Y., Zhang, H., & Li, Z. (2020). Role of surface latent heat flux in shallow cloud
608 transitions: A mechanism-denial LES study. *Earth and Space Science Open Archive*
609 *ESSOAr*.

610

611

612 **Figures:**

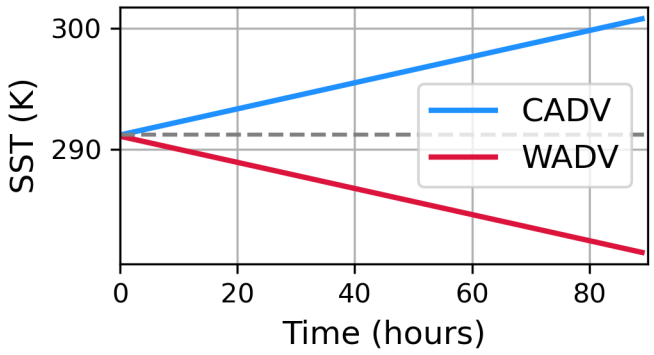

613

614 Figure 1: Time evolution of the sea surface temperature in the two simulations.

615

616

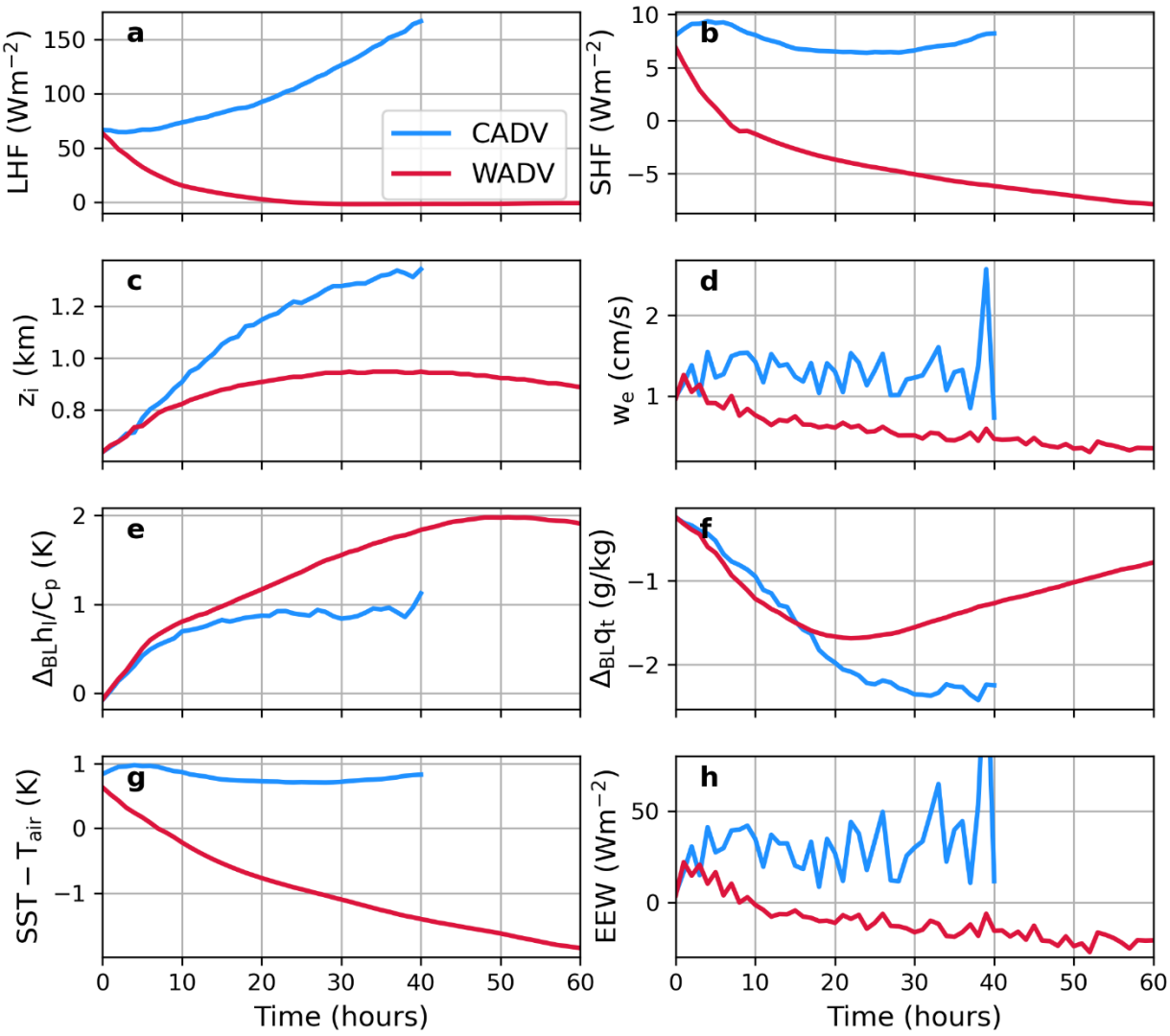

Figure 2: Time series of key variables of experiments CADV (blue) and WADV (red).

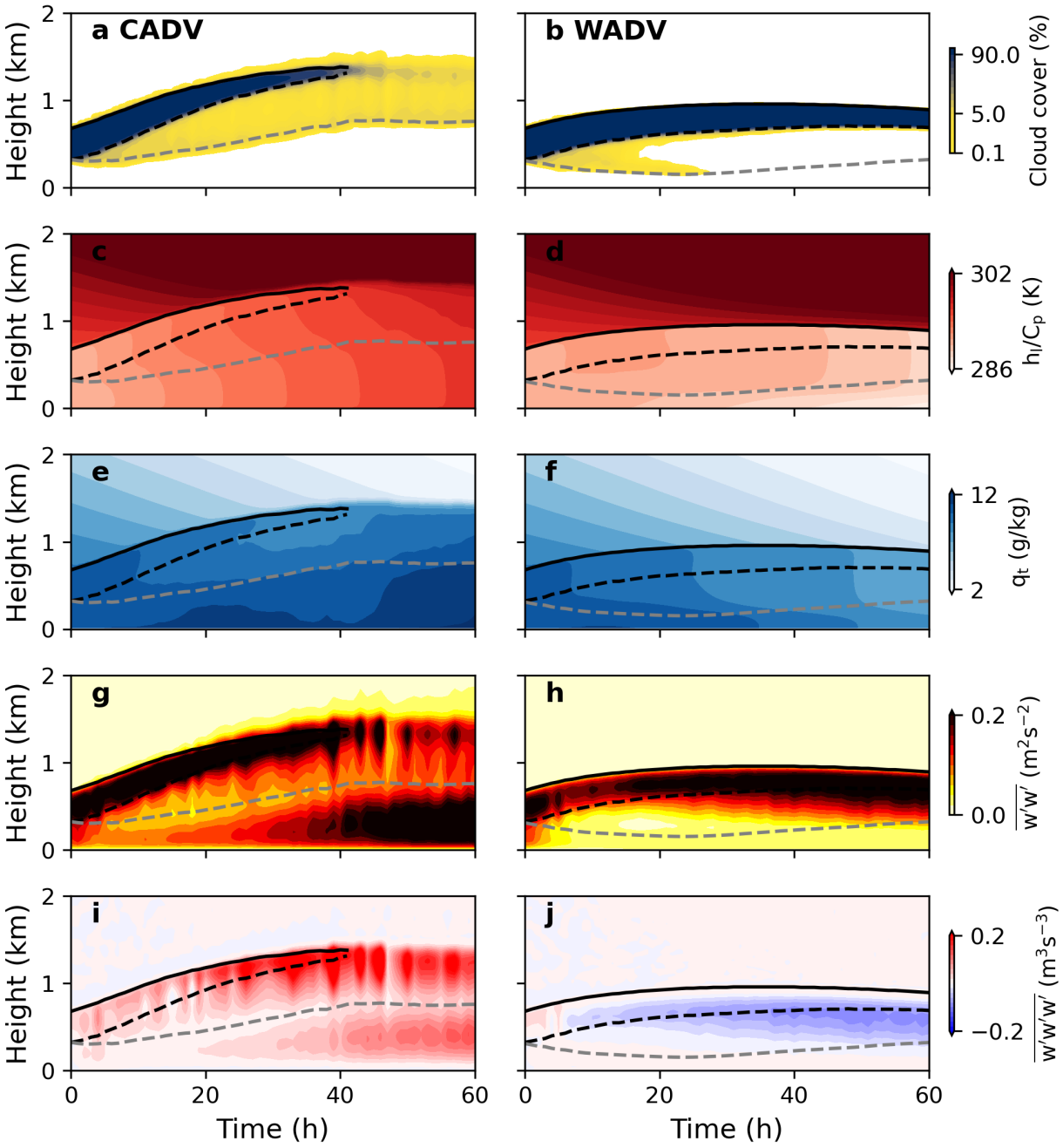

Figure 3: Time-height plots of key variables of experiments CADV (left) and WADV (right).

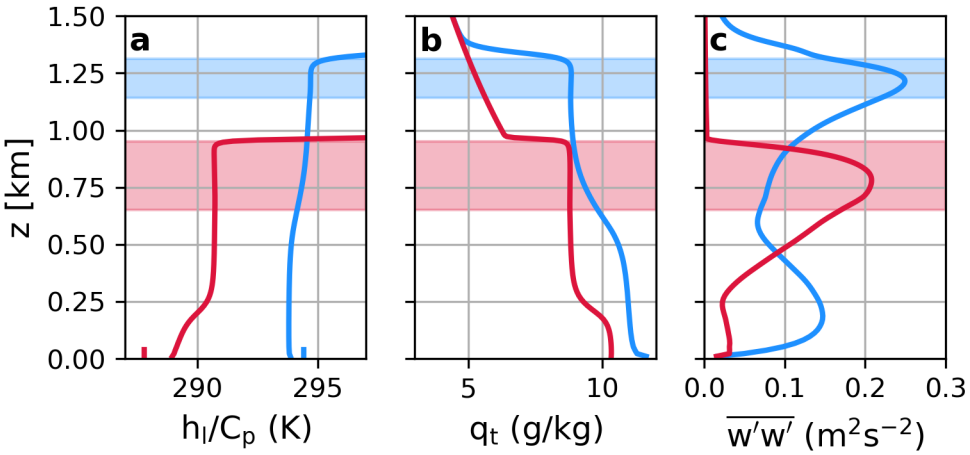

Figure 4: Profiles of h_l/C_p (a), q_t (b), and vertical velocity variance (c) for CADV (blue) and WADV (red) at t = 30 h. Ticks at the bottom of (a) are the sea surface temperatures.

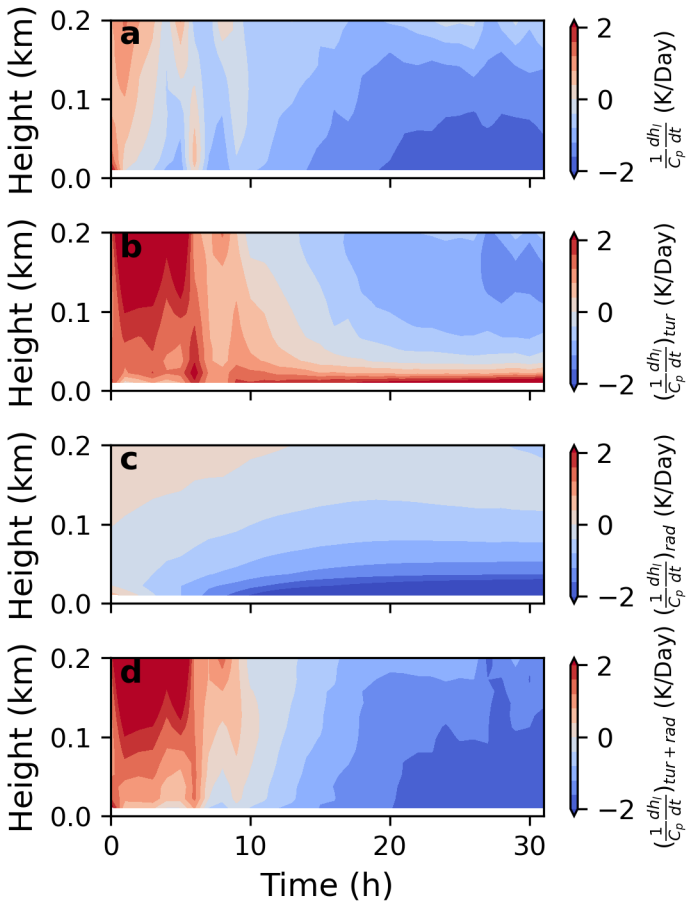

638

639 Figure 5: Time-height plots of total heating rate (a), heating rate due to turbulence (b),

640 heating rate due to radiation (c), and heating rate due to turbulence and radiation (d) for WADV.

641

642

643

644

645

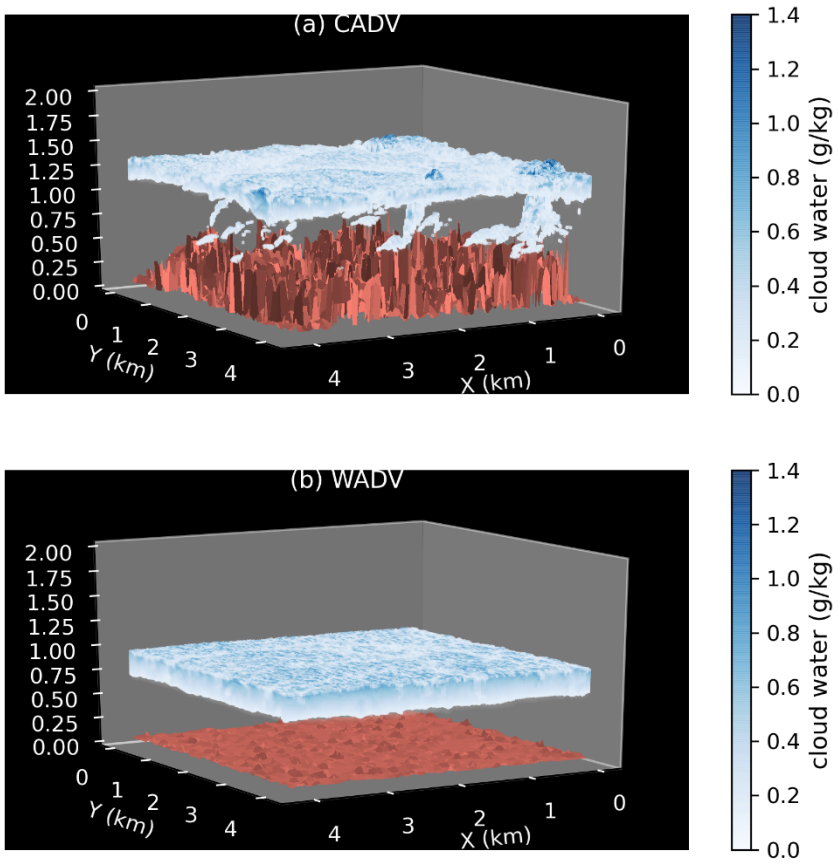

Figure 6: 3D visualizations of cloud liquid water content at t = 30 h for the CADV and WADV experiments. The red surfaces are the contours of the top 1% q_t in each column.

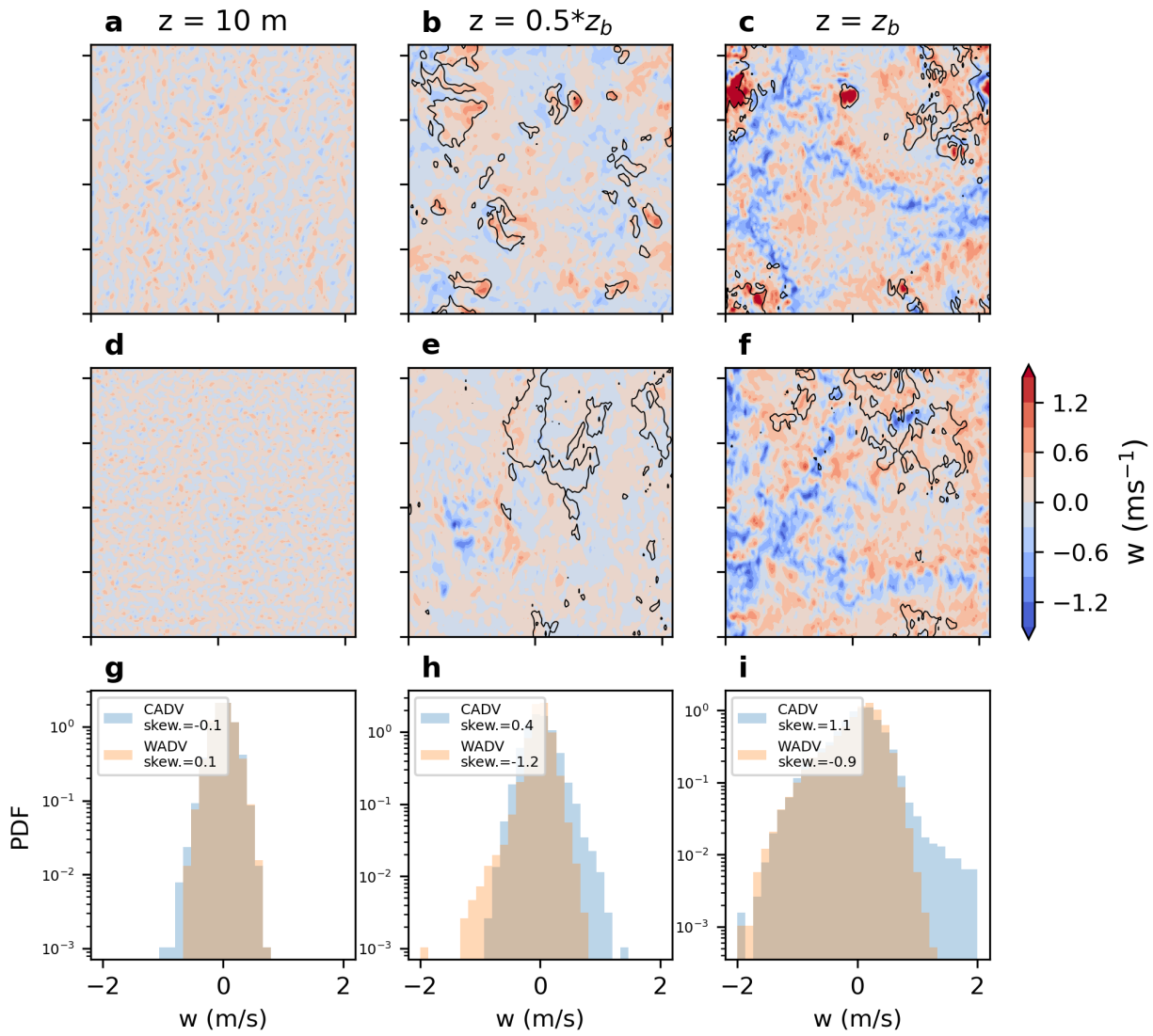

Figure 7: Vertical velocity field at z = 10 m (left), z = 0.5z_b (middle), and z = z_b (right) for the CADV (top) and WADV (middle). The bottom panel is the probability distribution functions of the vertical velocity for the two experiments. In (b), (c), (e), and (f), black contours correspond to the top 10% q_t in each horizontal layer.

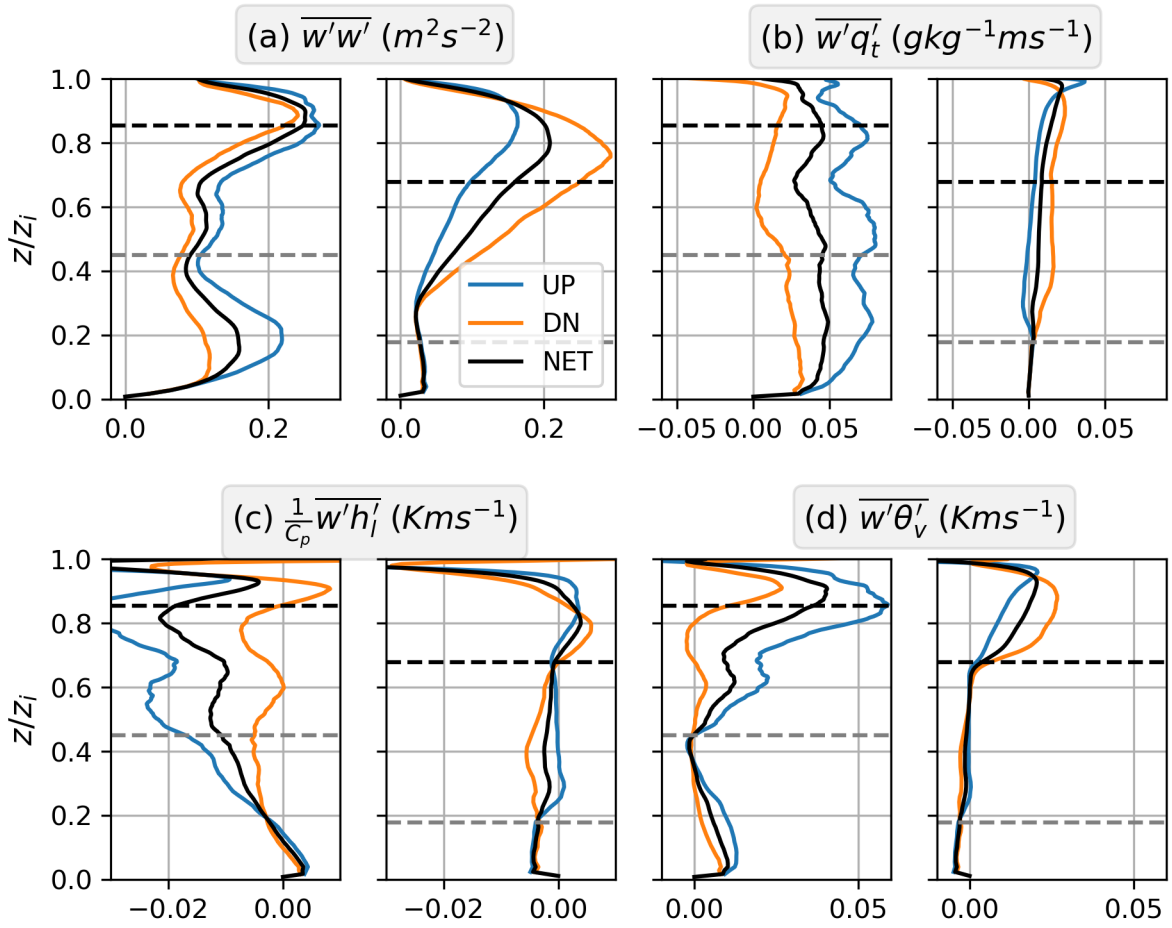

Figure 8: Vertical profiles of vertical velocity variance (a), moisture flux (b), heat flux (c), and buoyancy flux (d) of updrafts (blue) and downdrafts (orange) for CADV (left) and WADV (right). Horizontal black and grey dashed lines mark the base heights of stratocumulus decks and LCL, respectively.

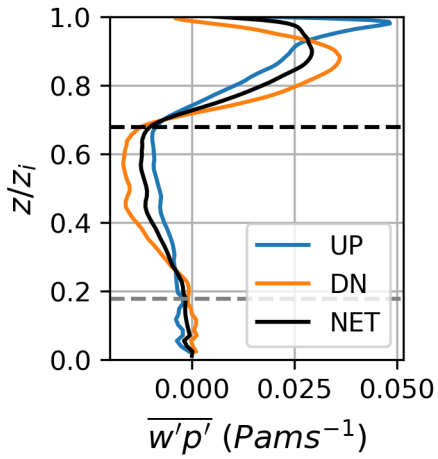

Figure 9: Vertical profiles of $\overline{w'p'}$ at t = 30 h in WADV.

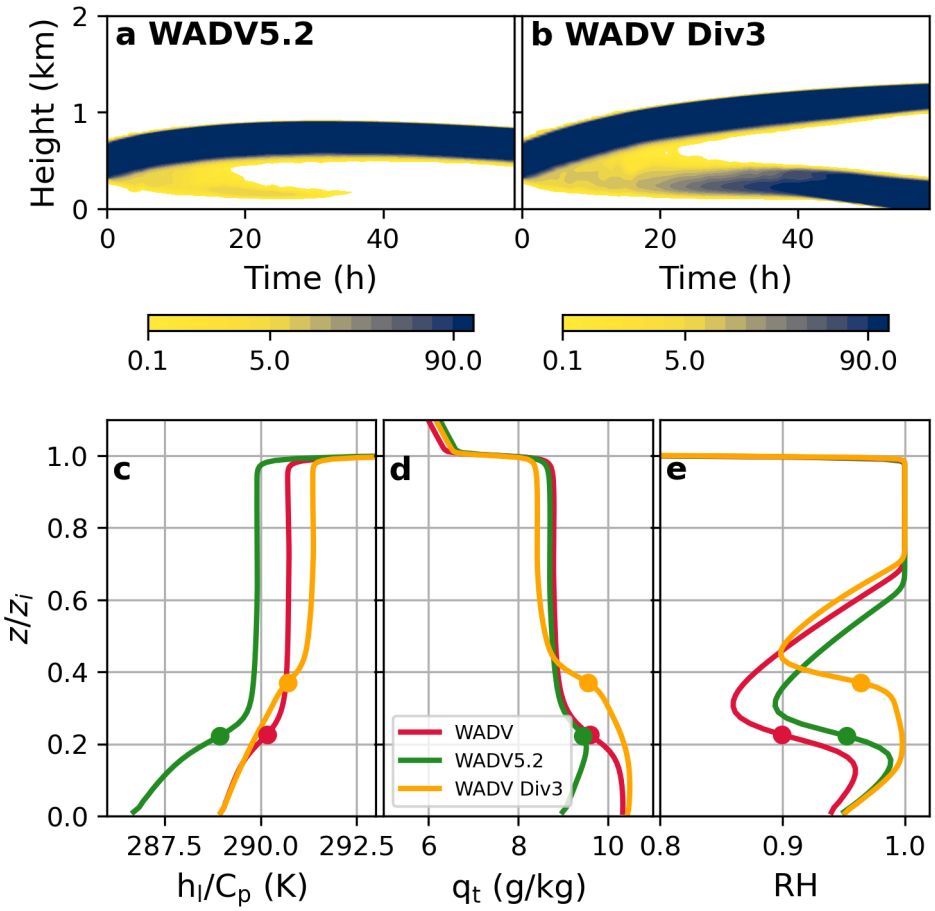

679

680 Figure 10: Time-height plots of cloud fraction for WADV5.2 (a) and WADV Div3 (b), and

681 vertical profiles of h_l/C_p (c), q_t (d), and relative humidity (e) for the WADV, WADV5.2, and

682 WADV Div3. The solid dots mark the z_{li}.

683

684

685

686

687

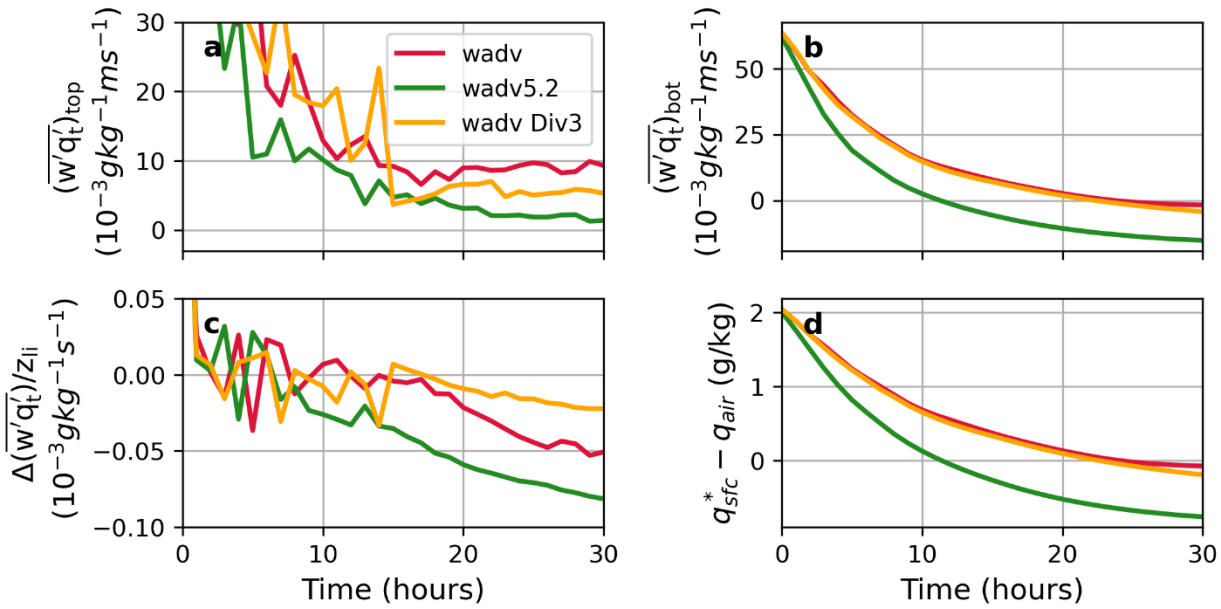

Figure 11: Time series of $(\overline{w'q_t'})_{top}$ (a), $(\overline{w'q_t'})_{bot}$ (b), $((\overline{w'q_t'})_{top}$ - $(\overline{w'q_t'})_{bot})/z_{li}$ (c), q_{sfc}^{*} - q_{air} (d) for the three WADV runs.